MOMO – V. Effelsberg, *Swift*, and *Fermi* study of the blazar and supermassive binary black hole candidate OJ 287 in a period of high activity

S. Komossa,[1]★ D. Grupe,[2] A. Kraus,[1] A. Gonzalez,[3] L. C. Gallo,[3] M. J. Valtonen,[4,5] S. Laine,[6] T. P. Krichbaum,[1] M. A. Gurwell,[7] J. L. Gómez,[8] S. Ciprini,[9,10] I. Myserlis [1,11] and U. Bach [1]

[1]*Max-Planck-Institut für Radioastronomie, Auf dem Hügel 69, D-53121 Bonn, Germany*
[2]*Department of Physics, Earth Science, and Space System Engineering, Morehead State University, 235 Martindale Dr, Morehead, KY 40351, USA*
[3]*Department of Astronomy and Physics, Saint Mary's University, 923 Robie Street, Halifax, NS, B3H 3C 3, Canada*
[4]*Finnish Centre for Astronomy with ESO, University of Turku, FI-20014, Turku, Finland*
[5]*Department of Physics and Astronomy, University of Turku, FI-20014, Turku, Finland*
[6]*IPAC, Mail Code 314-6, Caltech, 1200 E. California Blvd., Pasadena, CA 91125, USA*
[7]*Center for Astrophysics | Harvard & Smithsonian, Cambridge, MA 02138, USA*
[8]*Instituto de Astrofísica de Andalucía-CSIC, Glorieta de la Astronomía s/n, E-18008 Granada, Spain*
[9]*Istituto Nazionale di Fisica Nucleare (INFN) Sezione di Roma Tor Vergata, Via della Ricerca Scientifica 1, I-00133, Roma, Italy*
[10]*ASI Space Science Data Center (SSDC), Via del Politecnico, I-00133, Roma, Italy*
[11]*Institut de Radioastronomie Millimétrique, Avenida Divina Pastora 7, Local 20, E-18012, Granada, Spain*

ABSTRACT

We report results from our ongoing project MOMO (Multiwavelength Observations and Modelling of OJ 287). In this latest publication of a sequence, we combine our *Swift* UVOT–XRT and Effelsberg radio data (2.6–44 GHz) between 2019 and 2022.04 with public SMA data and gamma-ray data from the *Fermi* satellite. The observational epoch covers OJ 287 in a high state of activity from radio to X-rays. The epoch also covers two major events predicted by the binary supermassive black hole (SMBH) model of OJ 287. Spectral and timing analyses clearly establish: a new UV–optical minimum state in 2021 December at an epoch where the secondary SMBH is predicted to cross the disc surrounding the primary SMBH; an overall low level of gamma-ray activity in comparison to pre-2017 epochs; the presence of a remarkable, long-lasting UV–optical flare event of intermediate amplitude in 2020–2021; a high level of activity in the radio band with multiple flares; and particularly a bright, ongoing radio flare peaking in 2021 November that may be associated with a gamma-ray flare, the strongest in 6 yr. Several explanations for the UV–optical minimum state are explored, including the possibility that a secondary SMBH launches a temporary jet, but the observations are best explained by variability associated with the main jet.

Key words: galaxies: active – galaxies: jets – galaxies: nuclei – quasars: individual (OJ 287) – (galaxies:) quasars: supermassive black holes – X-rays: galaxies.

1 INTRODUCTION

Supermassive binary black holes (SMBBHs) form in the course of galaxy mergers. They are expected to be the loudest sources of low-frequency gravitational waves (GWs) in the Universe (Sesana 2021) and they are a key component in our understanding of galaxy evolution (Volonteri, Haardt & Madau 2003; Komossa, Baker & Liu 2016). The search for, and analysis of, SMBBHs in all stages of their evolution has therefore evolved into an important field in extragalactic astrophysics. The most evolved binaries are well beyond the 'final parsec' in their orbital evolution (Colpi 2014), where GW emission contributes to their orbital shrinkage. They have so far remained spatially unresolved with available imaging

techniques, and indirect methods are used for their search and identification.

Blazars are particularly suitable for searching sub-parsec binary systems, because of periodicity imprints on light curves due to beaming effects and on jet structures (Begelman, Blandford & Rees 1980), and many candidate binaries among blazars have been identified in recent years (e.g. Sillanpää et al. 1988; Graham et al 2015). Different mechanisms to explain semiperiodicities have been considered in blazars: apparent changes in the observed luminosity because of periodically varying Doppler boosting due to a precessing jet or due to an orbiting secondary SMBH, or true changes in the intrinsic luminosity due to disc impacts (tilted orbit of the secondary) or due to stream-feeding from circumbinary discs in systems without inner accretion disc (in-plane orbit of the secondary) (see de Rosa et al. 2019; Komossa et al. 2021b for reviews).

These signatures do not always uniquely imply a binary. For instance, disc precession around a single SMBH can lead to

★ E-mail: astrokomossa@gmx.de, skomossa@mpifr.de

semiperiodicity in light curves as well (Liska et al. 2018). Periodic jet structures can also arise around single SMBHs through helical magnetic fields and MHD instabilities (Rieger 2004; Lister et al. 2013). Therefore, multiwavelength observations and long-term monitoring efforts are required to distinguish between different possible causes of semiperiodicities (Valtonen et al. 2022).

Independent of the presence of any binary, blazars are excellent laboratories for understanding disc–jet physics (Blandford, Meier & Readhead 2019). Hence, detailed observations of individual, bright, nearby, and active systems are extremely important in furthering our understanding of the geometry and emission mechanisms of blazars in general and SMBBHs in particular.

OJ 287 is such a nearby, bright blazar (redshift $z = 0.306$, RA: $08^h54^m48^s.87$, Dec.: $+20°06'30''.6$) and among the best candidates to date for hosting a compact SMBBH. Its optical light curve was characterized by sharp and bright outbursts increasing flux more than tenfold, and lasting for months (Sillanpää et al. 1988). Optical maxima are double-peaked (Sillanpää et al. 1996). Based on the semiperiodic appearance of the bright maxima, several variants of SMBBH models were considered (e.g. Sillanpää et al. 1988; Lehto & Valtonen 1996; Katz 1997; Villata et al. 1998; Valtaoja et al. 2000; Liu & Wu 2002; Qian 2015; Britzen et al. 2018; Dey et al. 2018). The best-explored scenario, modelled in most detail and making predictions for future events, involves a binary with a massive primary SMBH of 1.8×10^{10} M$_\odot$, and a secondary SMBH of 1.5×10^8 M$_\odot$ on an eccentric, precessing orbit (Valtonen et al. 2016; Dey et al. 2018; Laine et al. 2020; Valtonen et al. 2022). The double-peaks in the optical light curve are explained as the times when the secondary SMBH impacts the disc around the primary twice during its 12.06 yr orbit ('impact flares' hereafter; Lehto & Valtonen 1996; Valtonen et al. 2019). The main flares do not become visible immediately, but only after the impact-driven bubbles expanding from the impact point (Ivanov, Igumenshchev & Novikov 1998) become optically thin.

OJ 287 is also a good example of a multimessenger source. In the binary scenario, GWs are expected to be detected directly with future pulsar timing arrays (PTAs; Yardley et al. 2010; Valtonen et al. 2022). OJ 287 is a bright and variable emitter across the whole electromagnetic spectrum. In the optical band, its brightest outbursts reached 12 mag, comparable to the brightness of one of the nearest quasars. OJ 287 is detected at VHE energies ($E > 100$ GeV) with VERITAS (O'Brien 2017) and in the gamma-ray regime with the *Fermi* (Abdo et al. 2009; Ballet et al. 2020). In X-rays, the first detection was with Einstein (Madejski & Schwartz 1988), then followed by observations with other major X-ray observatories [per observatory, presented first by Sambruna et al. (1994, EXOSAT), Comastri, Molendi & Ghisellini (1995, *ROSAT*), Idesawa et al. (1997, *ASCA*), Massaro et al. (2003, *Swift*), Ciprini et al. (2007, *XMM–Newton*), Massaro et al. (2008, BeppoSAX), Seta et al. (2009, *Ginga*), Marscher & Jorstad (2011, *Chandra*), Komossa et al. (2020, NuSTAR), and Prince et al. (2021, AstroSat), respectively].

Observations with *XMM–Newton* and the Neil Gehrels *Swift* observatory (*Swift* hereafter) over two decades established OJ 287 as one of the most spectrally variable blazars in the X-ray band (Komossa et al. 2020, 2021a, d). *XMM–Newton* spectroscopy has firmly established the presence of both a highly variable synchrotron and inverse Compton (IC) component, offering a unique chance of observing *both* components in the same soft X-ray band; rare in blazars (Komossa et al. 2020, 2021a). Outbursts in 2016/17 (Komossa et al. 2017) and 2020 (Komossa et al. 2020), discovered in the course of dedicated *Swift* monitoring of OJ 287, are driven by supersoft synchrotron flares (Komossa et al. 2020). NuSTAR discovered a

remarkable steep X-ray spectrum up to 70 keV (Komossa et al. 2020). OJ 287 hosts an extended X-ray jet detected with *Chandra* (Marscher & Jorstad 2011). Structure function analyses revealed characteristic time-scales of 4–39 d depending on waveband and activity state of OJ 287 (Komossa et al. 2021d).

OJ 287 is a strong and highly variable radio source and has been the target of past radio-monitoring efforts, including campaigns between 1972 and 1996 (Valtaoja et al. 2000), and it was part of a multifrequency radio monitoring campaign of a larger sample of *Fermi* AGN between 2007 and 2014 (Fuhrmann et al. 2016; Hodgson et al. 2017). OJ 287 was also subject of major concerted optical monitoring campaigns, including polarimetry at select epochs. These campaigns were essential in identifying the sharp double-peaks over decades and in developing the binary model (e.g. Smith et al. 1987; Sillanpää et al. 1988; Pursimo et al. 2000; Villforth et al. 2010; Valtonen & Sillanpää 2011; Pihajoki, Valtonen & Ciprini 2013a; Zola et al. 2016; Dey et al. 2018; Valtonen et al. 2022, and references therein), and in tracing the short-time variability characteristics with the Kepler mission (Wehrle, Carini & Wiita 2019). However, these important campaigns still lacked the broad-band coverage that is necessary to distinguish between various different thermal and non-thermal emission processes from the jet, the accretion disc and the binary at all times. For instance, optical polarization can be variable in both scenarios; mixtures of thermal and non-thermal emission on the one hand, and pure non-thermal shocks in jets on the other hand. Gamma-ray and radio monitoring traces the non-thermal emission well but misses thermal components as well as the non-thermal spectral energy distribution (SED) around its peak. Further, the SMBBH model continues to make new predictions that can only be tested in future observations (e.g. Valtonen et al. 2022).

Therefore, the programme MOMO (Multiwavelength Observations and Monitoring of OJ 287) was initiated in late 2015 (e.g. Komossa et al. 2021c). The 100m radio telescope at Effelsberg and the Neil Gehlrels *Swift* observatory are at the heart of the project and are combined with deep follow-up multiwavelength spectroscopy and public gamma-ray observations. Together they cover frequencies between 2 GHz and 100 GeV. MOMO provides broad-band SEDs, light curves and spectra in all activity states of OJ 287.

This paper is the latest in a sequence reporting about MOMO results. Here, we present Effelsberg and *Swift* observations between 2019 January and 2022 January, covering several epochs of exceptional binary and/or jet activity. This paper is structured as follows. In Section 2, we introduce the MOMO project; its key goals, its set-up and the main results obtained so far. In Section 3, we present the analysis and results from the *Swift* data. The Effelsberg multifrequency radio data and results are given in Section 4. The discussion is presented in Section 5 with focus on epochs of exceptional flux or spectral states, and epochs of predicted binary activity. Summary and conclusions are provided in Section 6. Throughout this paper we use a cosmology with $H_0 = 70$ km s^{-1} Mpc^{-1}, $\Omega_M = 0.3$, and $\Omega_\Lambda = 0.7$. At the distance of OJ 287, this corresponds to a scale of 4.5 kpc arcsec^{-1} (Wright 2006).

2 MOMO PROJECT

2.1 Programme description and previous results

The programme MOMO consists of dedicated, dense, long-term flux and spectroscopic monitoring and deep, higher sensitivity follow-up observations of the blazar OJ 287 at >13 frequencies from the radio to the high-energy band (see Komossa et al. 2021c for an overview). It was initiated in late 2015. In particular, we are using *Swift* to cover

the optical and UV bands in six filters as well as the 0.3–10 keV X-ray band, and we are using the 100m Effelsberg radio telescope to acquire radio measurements between 2.6 and 44 GHz. Public gamma-ray data from the *Fermi* satellite are added. Deep follow-up observations are triggered at exceptional activity states or at particular epochs including *XMM–Newton*, NuSTAR, and spectroscopy at ground-based optical telescopes. A few single observations are conducted quasi-simultaneous with the Event Horizon Telescope (EHT; Event Horizon Telescope Collaboration 2019) observations of OJ 287.

MOMO represents the densest long-term monitoring of OJ 287 involving X-rays and broad-band SEDs to date. The monitoring cadence is as short as 1 d in cases of outbursts or other noteworthy flux, spectral, or polarimetry states of OJ 287, and is typically 3–4 d in the X-ray–UV–optical bands, and three weeks in the radio bands. The theoretical part of the project aims at understanding jet and accretion physics of the blazar central engine in general and the supermassive binary black hole scenario in particular.

Results are presented in a sequence of publications and so far included: (1) the detection and detailed analysis of two major non-thermal X-ray–UV–optical outbursts in 2016/17 and 2020 (Komossa et al. 2017, 2020) and the analysis of the complete long-term *Swift* light curve at all activity states of OJ 287 (Komossa et al. 2021d); (2) *Swift*, *XMM–Newton*, and NuSTAR spectroscopy of the 2020 outburst around maximum, clearly establishing the spectral components up to ∼70 keV, including a giant soft X-ray excess of synchrotron origin and an unexpectedly steep spectrum in the NuSTAR band out to 70 keV (Komossa et al. 2020); (3) interpretation of selected events in the context of the binary black hole scenario of OJ 287 (Komossa et al. 2020, 2021b); (4) the detection of highly variable radio polarization during the first year of our Effelsberg monitoring in late 2015 and 2016 (Komossa et al. 2015; Myserlis et al. 2018); (5) the identification of characteristic and correlated variability across SEDs (Komossa et al. 2017, 2021c); (6) *XMM–Newton* and *Swift* spectroscopy during EHT campaigns in 2018, and a comprehensive analysis of all *XMM–Newton* spectra of the last two decades (Komossa et al. 2021a); (7) the identification of characteristic optical–UV-X-ray time lags in the range of 0–17 d based on discrete cross-correlation functions, and estimates of BLR and torus size of OJ 287 to constrain external Comptonization models (Komossa et al. 2021d).

All *Swift* data obtained by us are analysed within days. The community is alerted in form of *Astronomer's Telegrams* about noteworthy events like outbursts or deep minimum states of OJ 287 we detect with *Swift* or with the Effelsberg telescope (ATel #8411, #9629, #9632, #10043, #12086, #13658, #13702, #13785, #14052, #15145). That way, additional multiwavelength observations can be triggered by the community that are not covered by the MOMO programme.

Further details of the project data bases and observation strategies with *Swift* and with the Effelsberg telescope are given below in the respective subsections.

2.2 Project data base: MOMO-radio

In the radio regime, we are using the 100m Effelsberg radio telescope. It offers multiple advantages: a broad frequency range, a large number of receivers at the secondary focus and a high sensitivity. Our monitoring of OJ 287 in the course of the MOMO-radio project started in 2015 December. Flux and spectral measurements at a dense cadence of typically 3 weeks are obtained (programme identifications 99-15, 19-16, 12-17, 13-18, 75-19, and 65-20, 70-21), covering frequencies between 2.6 and 44 GHz.

In the radio regime, a coverage of OJ 287 is possible even at that particular epoch each year when OJ 287 is unobservable with ground-based optical telescopes and with *Swift* due to its solar proximity. The Effelsberg telescope can still observe sources at projected distances of only a few degrees from the Sun (albeit with some occasional degradation of signal quality).

Radio emission traces the synchrotron emission components. The ongoing measurements are used to (1) obtain flux densities and polarization and their evolution, including the time intervals around predicted binary impact flares and after-flares; (2) time the radio high-state(s), especially with respect to the multiwavelength data obtained in the MOMO programme; (3) measure the evolution of jet emission and magnetic fields; and (4) distinguish between different SMBBH scenarios and test new predictions of the best-developed binary model, based on distinctly different predictions in the radio regime for the first and second optical peak of the double peaks and for the after-flares. For instance, major optical flares will not be accompanied by radio flares if they are thermal in nature.[1] If instead both optical peaks are of synchrotron origin, then two radio flares are expected with a polarization evolution that follows synchrotron theory.

2.3 Gamma-ray band

The MOMO project was designed with the availability of *Fermi* LAT (Large Area Telescope) gamma-ray data in mind. Unlike the *Swift* and Effelsberg observations that are proposed and analysed by us, the gamma-ray data were retrieved from the *Fermi* archive. They extend the light curve and SED coverage of OJ 287 into the 0.1–100 GeV regime. Publicly available *Fermi* LAT (Atwood et al. 2009) data of OJ 287 in the gamma-ray band were retrieved from the *Fermi*-LAT light-curve repository (Kocevski et al. 2021).[2] Weekly averages of the fluxes, and the spectral model with a fixed photon index of 2.16 of a logarithmic parabolic power-law model (logpar) description, were used. This description is preferred in our case over variants of free index fits (e.g. Hodgson et al. 2017; Kapanadze et al. 2018), because OJ 287 remains in a low gamma-ray state most of the time during the epoch of interest, and fits with free index come with large errors that can introduce spurious luminosity variations in low states. For any flare states mentioned in the text, we have checked that their identification remains robust when using a free-index fit instead.

2.4 MOMO-UO and MOMO-X

To cover the optical to X-ray bands, we have used the versatile space mission *Swift* because of its broad-band coverage, its high sensitivity, and its scheduling flexibility and fast response time (Gehrels et al. 2004).

High-cadence light curves and SEDs of OJ 287 are obtained at a cadence that is denser during outbursts (1–3 d), and sparser during more quiescent epochs (3–7 d) with longer gaps when OJ 287 remained constant for several subsequent observations. Occasional gaps in the cadence can also be due to the scheduling of a higher priority target (mostly GRBs), and gaps also arise when OJ 287 is unobservable with *Swift* due to its close proximity to the moon (∼3–4 d each) or the Sun (∼3 months each year). Exposure times are in

---

[1]Except for the epochs, when the secondary SMBH may undergo accretion events in conjunction with launching a short-lived jet (Pihajoki et al. 2013b; Dey et al. 2021).

[2]https://fermi.gsfc.nasa.gov/ssc/data/access/lat/LightCurveRepository/

Table 1. Log of our *Swift* observations between 2019 January and 2022 January 15 with observation ids (OBSIDs) 34934-174 to 35905-187. The central wavelengths of the UVOT filters (Poole et al. 2008) are reported in the third column and the durations of the single-epoch observations are given in the fourth column.

Instrument	Filter	Waveband/central wavelength	Δt (ks)
XRT		0.3–10 keV	0.3–2
UVOT	W2	1928 Å	0.12–0.6
	M2	2246 Å	0.09–0.5
	W1	2600 Å	0.06–0.3
	U	3465 Å	0.03–0.16
	B	4392 Å	0.03–0.16
	V	5468 Å	0.03–0.16
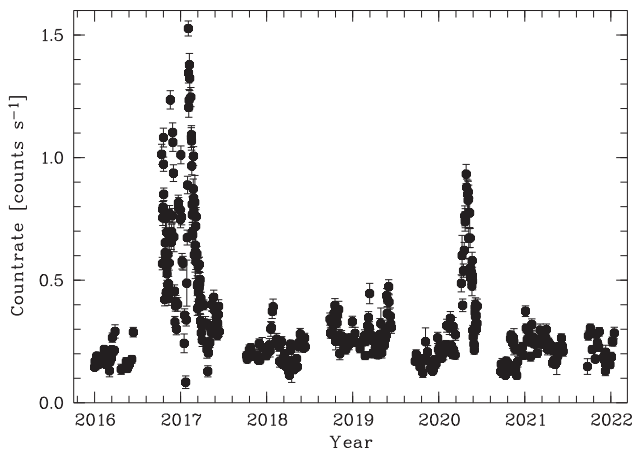
Figure 1. *Swift* XRT light curve of OJ 287 between 2016 January and 2022 January.

the range of 0.3–2 ks in X-rays – typically 2 ks when OJ 287 was faint, typically 1 ks when it was bright (Table 1 and Fig. 1). Exposure times for the UV–optical telescope (UVOT) are in the same range as the X-ray observations.

While the MOMO project started in late 2015, multiwavelength archival data are added when needed to analyse long-term trends. This includes *Swift* data taken between 2005 and 2015 (Massaro et al. 2008; Stroh & Falcone 2013; Williamson et al. 2014; Valtonen et al. 2016; Komossa et al. 2017; Siejkowski & Wierzcholska 2017) and it includes occasional later *Swift* data sets not from the MOMO programme.

Here, we present our most recent *Swift* data of OJ 287 from 2021 and up until 2022 January 15. After that date, *Swift* went into safe mode for a month. We also add the period 2019–2020 (Komossa et al. 2020, 2021d), for joint analysis with the Effelsberg radio data and *Fermi* gamma-ray light curve. Further details of the data acquisition and analysis in each waveband are reported in the next Sections.

2.5 Additional Submillimetre Array data

1.3 mm (225 GHz) flux density data were obtained at the Submillimetre Array (SMA) near the summit of Maunakea (Hawaii). These observations are not part of the MOMO programme, but are added here to extend the radio observations to higher frequencies. OJ 287 is included in an ongoing monitoring program at the SMA to determine the fluxes of compact extragalactic radio sources that can be used as calibrators at mm wavelengths (Gurwell et al. 2007). Observations of available potential calibrators are from time to time

observed for 3–5 min, with the measured source signal strength calibrated against known standards, typically Solar system objects (Titan, Uranus, Neptune, or Callisto). Data from this programme are updated regularly and are available at the SMA website.[3]

3 *SWIFT* DATA ANALYSIS AND RESULTS

3.1 *Swift* XRT data analysis

Swift data reduction follows the same procedures we used before (e.g. Komossa et al. 2020, 2021d). In brief, the X-ray telescope (XRT) data analysis was performed using the XRTDAS package developed at the ASI Science Data Center (SSDC) and included in the HEASOFT package (version no. 6.28). During the majority of the observations, the *Swift* XRT (Burrows et al. 2005) was operating in *photon counting* (PC) mode (Hill et al. 2004). Above a source count rate of ~1 ct s^{-1}, observations were done in *windowed timing* (WT) mode (Hill et al. 2004), where only the central 4×4 arcminutes of the CCD are read out. This procedure serves to minimize the effect of photon pile-up. X-ray count rates in the energy band 0.3–10 keV were determined making use of the XRT product tool at the *Swift* data centre in Leicester (Evans et al. 2007).

To carry out the timing and spectral analysis, we selected source photons within a circular area of a radius of 20 detector pixels. One pixel is equivalent to a scale of 2.36 arcsec. Because of the required source extraction size, the X-ray jet of OJ 287 detected with *Chandra* (Marscher & Jorstad 2011) is included in the area. However, at a corresponding *Swift* XRT count rate of only 0.009 cts s^{-1}, its contribution to the integrated emission is negligible in all observed X-ray activity states of OJ 287. The background photons were extracted in a nearby circular region with a radius of 236 arcsec.

We note that OJ 287 was off-axis in most of the *Swift* XRT data sets. This is typical for *Swift* monitoring observations. However, the *Swift* point spread function (PSF) does not strongly depend on the location within the inner field of view (Moretti et al. 2005).

The effect of photon pile-up affects data above a count rate of ~0.7 cts s^{-1}. To correct for it, we first created a region file where the inner circular area of the PSF was excluded from the analysis. Then, the loss in counts is corrected by creating a new ancillary response file that is used in XSPEC to correct the flux measurement.

X-ray spectra of the source and background in the energy band 0.3–10 keV were generated and the spectral analysis was carried out with the package XSPEC (version 12.10.1f; Arnaud 1996). Except when noted otherwise, spectral fits were done with the unbinned data and using the W-statistics of XSPEC. The X-ray count rate light curve of OJ 287 until 2022 January 15 is shown in Fig. 1.

3.2 *Swift* UVOT data analysis

We have also employed the *Swift* UVOT (UVOT; Roming et al. 2005) to observe OJ 287 in all three optical and all three UV photometric bands (see Table 1 for the filter central wavelengths). Here, we focus on data between 2019 and 2022.04, we have obtained in the course of the MOMO project. The use of all six filters ensures a dense coverage of the SED. This is important since OJ 287 varies rapidly, and epochs of correlated and uncorrelated variability across the optical-to-X-ray bands have been identified previously (Komossa et al. 2020, 2021d).

[3]http://sma1.sma.hawaii.edu/callist/callist.html

Exposure times of the UVOT are in the range of 0.3–2 ks. Most of the time, the UVOT bands V:B:U:W1:M2:W2 are observed with a ratio of 1:1:1:2:3:4 of the total exposure time, respectively (e.g. Grupe et al. 2010). There are occasional exceptions when the observation is interrupted by a high-priority target-of-opportunity (ToO) observation.

For further analysis, the observations in each filter were first co-added, making use of the tool UVOTIMSUM. In all six filters source counts were then extracted in a region of circular size and with an extraction radius of 5 arcsec centred on OJ 287. A nearby area of 20 arcsec radius was used to extract the background region. The tool UVOTSOURCE was used to measure magnitudes. Background-corrected counts were converted into VEGA magnitudes and fluxes, making use of the latest calibration (Poole et al. 2008; Breeveld et al. 2010). All fluxes are reported as flux density multiplied by the central frequency of the corresponding UVOT filter. For data since 2017, CALDB update version 20200925 was employed.[4]

UVOT data were corrected for Galactic reddening based on the reddening curves of Cardelli et al. (1989) and using $E_{(B-V)} = 0.0248$ (Schlegel, Finkbeiner & Davis 1998) and a correction factor in each filter according to equation (2) of Roming et al. (2009).

3.3 X-ray spectra

Spectra were fit with single power laws of photon index Γ_X (defined as $N(E) \propto E^{-\Gamma}$), adding Galactic absorption with a column density $N_{H, Gal} = 2.49 \times 10^{20}$ cm^{-2} (Kalberla et al. 2005) and using the absorption model TBABS (Wilms, Allen & McCray 2000). A single power law is the optimal spectral model to analyse single-epoch *Swift* data as the short observations do not well constrain multicomponent models, and the power-law description has been well established as a reliable measure of the X-ray spectral state of OJ 287 below 10 keV. Further, detailed spectral analysis of all high-sensitivity *XMM–Newton* data of OJ 287 (Komossa et al. 2021a) has shown that excess cold absorption is not required to fit the X-ray spectra of OJ 287.

Between 2019 and 2021, photon indices are in the range $\Gamma_X = 1.7$–2.8 (Fig. 2) with a trend of steeper indices as OJ 287 becomes X-ray brighter during high-states; a trend that was recognized before (e.g. Komossa et al. 2017, 2021d). A possible exception is the epoch in 2021 December where Γ_X shows an indication of steepening while the count rate decreases. However, this trend needs to be confirmed in ongoing monitoring, as measurement errors of single-epoch photon indices are large.

3.4 *Swift* light curves

The UVOT light curve during late 2020 to 2021 (Fig. 2) shows a long-lasting systematic rise and fade (referred to as 'broad flare'), starting in 2020 September from a low-state and with a first maximum in 2021 January and a second in March, then declining on the time-scale of months. Mini-flaring of small amplitude is superposed. While the amplitude of the event does not reach that of the 2020 April–June outburst, the event is of much longer duration. After the *Swift* Sun constraint, from 2021 September to November, high-amplitude mini-flaring (> 1 mag in the UV–optical) is then followed by a deep low-state in the UV–optical in December with fluxes as low as 16 mag in the UV (W2) and the optical (V); ~3 mag fainter than during the peak of the 2020 April–June outburst.

3.5 Discrete correlation function

Since the period 2020 September to 2021 June shows an interesting broad flare with mini-flare sub-structure in the UV–optical, we have expanded our previous discrete correlation function (DCF) analysis that covered the years 2015–2020 (Komossa et al. 2021d) and now apply it in the same way to the latest epoch. The time interval 2020 September to 2021 June, between two *Swift* Sun constraints, is analysed and we search for correlations between the optical *V* band and the UV *W*2 band.

The DCF technique is used to analyse unevenly sampled data sets (Edelson & Krolik 1988). We calculated the DCFs based on the prescription of Edelson & Krolik (1988) using the R package sour[5] (Edelson et al. 2017). The time-step τ over which the DCFs were computed corresponds to twice the median time-step across the September–June light curve. To evaluate the significance level of the measured lags, confidence contours for each DCF were produced by simulating $N = 10^3$ artificial W2 light curves. The prescription of Timmer & König (1995) was adopted, assuming a power spectral density of $P(f) \propto f^{-\alpha} = f^{-3}$ based on the results of the structure function (SF) analysis for W2 (Komossa et al. 2021d), taking $\alpha = \beta + 1$, where β is the SF slope. Artificial DCFs were then computed based on these artificial light curves, allowing for the computation of the 90th, 95th, and 99th percentiles based on the distribution of artificial DCFs at each time-step.

To evaluate the error of the lag measurements, the autocorrelation function (ACF) of the *W*2 light curve was computed, following the same procedure described above to create confidence contours for the ACF. Because the ACF peaks at $\tau = 0$ days, we estimated the error on the lag measurement as all ACF values in excess of the 99th percentile contour around $\tau = 0$ days. Measured lags are determined as those times where the DCF exceeds the 99th percentile contour for either an anticorrelation or a correlation. The times for which a lag measurement is reported are restricted to times corresponding to $\leq 1/3$ the length of each light curve. We find that the *V* and *W*2 light curves are closely correlated with a lag of 0 ± 7.5 d (Fig. 3).

3.6 Fractional rms variability amplitude

The fractional rms variability amplitude F_{var} (Vaughan et al. 2003) was computed for the two most recent *Swift* epochs, separately for each UVOT filter and in the X-ray band. F_{var} is defined as

$$F_{var} = \sqrt{\frac{S^2 - \overline{\sigma_{err}^2}}{\overline{x}^2}}, \tag{1}$$

where S^2 is the variance of the light curve, $\overline{\sigma_{err}^2}$ is the mean square of the measurement uncertainties, and $\overline{x}$ is the mean flux. The error of F_{var} was computed following appendix B of Vaughan et al. (2003) as

$$\sigma_{F_{var}} = \sqrt{\left(\sqrt{\frac{1}{2N}} \frac{\sigma_{err}^2}{\overline{x}^2 F_{var}}\right)^2 + \left(\sqrt{\frac{\sigma_{err}^2}{N}} \frac{1}{\overline{x}^2}\right)^2}, \tag{2}$$

where N is the number of datapoints used in the computation of F_{var}.

The fractional variability is similar in all optical and UV bands and slightly enhanced w.r.t. the X-ray band. Results are reported in Table 2.

---

[4]https://www.swift.ac.uk/analysis/uvot/index.php

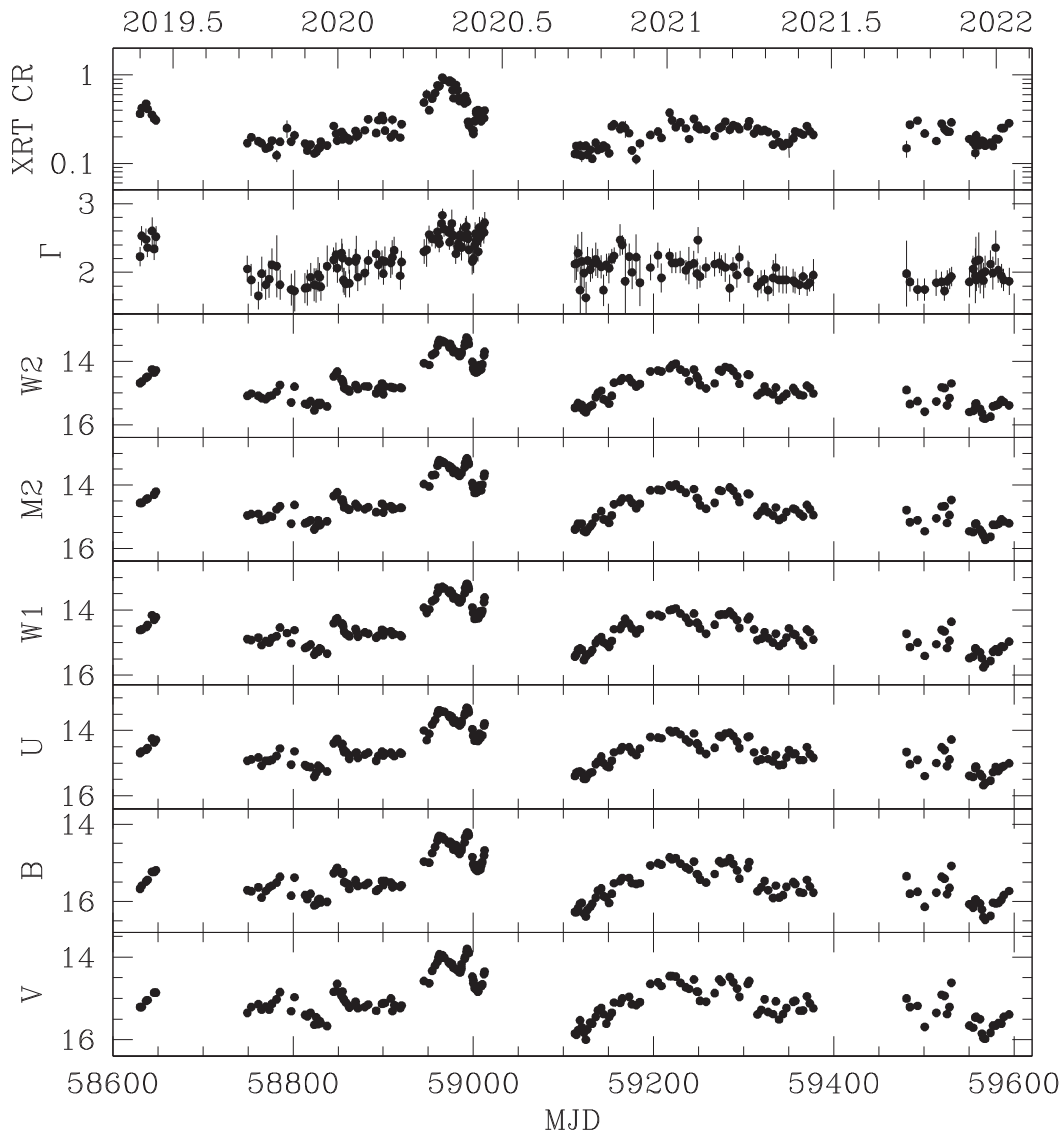[5]Available at https://github.com/svdataman/sour.

Figure 2. Observed *Swift* X-ray to optical light curve of OJ 287 since mid-2019 obtained in the course of the MOMO programme. The X-ray count rate is reported in cts s^{-1}. The UV–optical filter magnitudes are reported in the VEGA system, and are the directly observed values not yet corrected for Galactic extinction. Γ_X is the X-ray photon index from single power-law spectral fits. The two long gaps in the light curves correspond to epochs when OJ 287 is unobservable with *Swift* due to its projected proximity to the Sun. The last data point is from 2022 January 15.

4 EFFELSBERG MULTIFREQUENCY RADIO OBSERVATIONS

4.1 Data acquisition and reduction

Observations were obtained between 2.6 and 44 GHz switching between up to six receivers (Table 3). The cadence of observations was 3–4 weeks, or higher at selected epochs. Depending on weather conditions, the coverage at the highest frequencies was more sparse.

We note that the coverage of OJ 287 in mid-2019 (late July to August) was affected by the close proximity of OJ 287 to the Sun. In particular, at the time closest to the predicted binary impact flare and the Spitzer monitoring (Laine et al. 2020), the Effelsberg observation of OJ 287 could not be conducted because the painting of the structural parts was renewed. With the paint just removed and OJ 287 only a few degrees away from the Sun at the time interval in question, the extra reflectivity of the telescope support structure hindered the observation.

The cross-scan method (Heeschen et al. 1987; Kraus et al. 2003) was used to acquire the radio data. In the cross-scans, the telescope was moved in two perpendicular directions, azimuth and elevation, with the target source position at the centre of the scans. The number of sub-scans varied between 2–3 per direction for the low and 12–16 for the high frequencies. The observing time needed to measure the flux densities at all frequencies once was 25 min.

The data reduction and analysis was performed in a standard manner as described in, e.g. Kraus et al. (2003). In a first analysis step, a Gaussian profile was fit to the data of every single sub-scan. Bad sub-scans (for instance due to high pointing errors, radio frequency interference (RFI), or – in case of OJ 287 – disturbances by solar radiation around August 1 of each year) were identified and excluded from further analysis. After correcting for small pointing errors of the telescope, the amplitudes of the individual sub-scans were averaged. In some cases, at the highest frequencies and in mediocre weather conditions, the sub-scans of one direction (azimuth/elevation) were
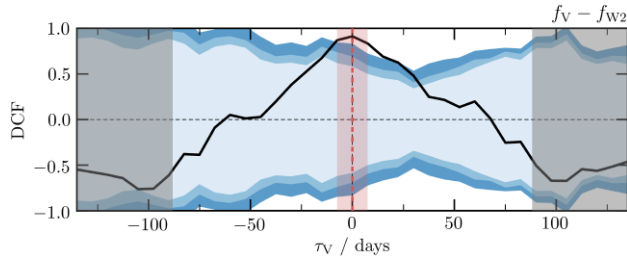
Figure 3. $V-W2$ DCF of OJ 287 for the epoch 2020 September to 2021 June (black line). Filled regions indicate the $\pm$90th (light blue), $\pm$95th (blue), and $\pm$99th (dark blue) percentiles from the light-curve simulations. The horizontal dashed line marks zero correlation and the vertical dashed line indicates $\tau_V = 0$ days. Positive τ_V values indicate V leading $W2$, negative values indicate lagging. Grey regions are between one-third to one-half the total light-curve length, where results become more unreliable. The vertical red line marks the measured time lag and its error. UV and optical fluxes are closely correlated with a lag consistent with zero days.

Table 2. Fractional variability amplitude F_{var} of the *Swift* UVOT and XRT fluxes of OJ 287 during 2020–2021.

	Epoch 6 2020 September – 2021 June	Epoch 7 2021 September–December
f_X	0.254 ± 0.011	0.28 ± 0.02
f_{W2}	0.375 ± 0.005	0.32 ± 0.01
f_{M2}	0.380 ± 0.006	0.34 ± 0.01
f_{W1}	0.374 ± 0.005	0.36 ± 0.01
f_U	0.369 ± 0.005	0.38 ± 0.01
f_B	0.374 ± 0.004	0.37 ± 0.01
f_V	0.362 ± 0.006	0.37 ± 0.01

averaged before the fitting of the Gaussian profile to increase the signal to noise ratio. Next, corrections for the atmosphere's opacity were applied as well as for the gain-elevation effect (change of sensitivity with elevation). Finally, absolute flux calibration was achieved by comparing the observed antenna temperatures with the expected flux densities of selected calibrators like 3C 286.[6] A detailed description of the analysis procedures will be given by Kraus et al. (in preparation).

The measurement uncertainties are based on the errors resulting from the least squares fit of the Gaussian profiles and statistical errors from averaging of the data. These errors are propagated throughout the data reduction process and combined with a final contribution which reflects the apparent residual fluctuations of the calibrators. At frequencies below 15 GHz, the final relative uncertainties are usually well below 5 per cent. The errors increase at higher frequencies due to the increased influence of weather effects, but are mostly of the order of 5–10 per cent.

4.2 Radio light curves

OJ 287 is found at a high level of activity in the radio band. Radio light curves (Fig. 4) show four separate main maxima in 2019 June,

[6]We note in passing that the radio calibrator 3C 286 has recently shown variability in the gamma-ray and X-ray band (Yao & Komossa 2021) opening the possibility of radio-variability of the inner jet, too. However, the bulk of the radio emission of 3C 286 is widely extended and 3C 286 is at high redshift, and therefore low-resolution radio observations as the ones carried out here will be unaffected by any variability of the inner jet emission.

2020 March, 2021 March, and 2021 November (dates are based on observations at $\nu = 36$ GHz; Table 4). The maxima are detected at all frequencies but are more pronounced at higher frequencies where sometimes additional substructure is evident. Based on the highest and lowest flux density measured during the whole epoch of observations, the total amplitude of variability is a factor of 1.67 (2.6 GHz), 1.96 (10.45 GHz), and 2.50 (36 GHz).

The single sharpest and the brightest flare, starting to rise in late 2021 July, approximately doubled its flux density in 135 d between $S = 3.82$ Jy at low state and 8.28 Jy at maximum (36 GHz). The flare maximum was reached at the highest frequencies first. After the peak in 2021 November the flux densities declined in December, but remained at high emission levels.

4.3 Radio SEDs

Radio SEDs are displayed in Fig. 5. They are highly variable and show a range of turn-over frequencies between 10 and 25 GHz. Radio spectral indices, defined as $f_\nu \propto \nu^{\alpha_\nu}$, vary between $\alpha_\nu = 0.17$ and 0.65 (in the band 2.6–10.45 GHz) and between $\alpha_\nu = -0.38$ and 0.23 (10.45–36 GHz).

In mid-2019, an inversion of the radio spectrum is seen where high frequencies show similar flux density levels as those at 4.85 GHz. Flux densities at 36 GHz reach particular low values.

4.4 Broad-band light curves

Fig. 6 compares the Effelsberg, SMA, *Swift*, and *Fermi* light curves between 2019 and 2022 January. Weekly averages of the *Fermi* fluxes were used and constant index of the logarithmic parabolic model (see Section 2.3) was assumed. The first radio flare falls within an epoch when OJ 287 was unobservable with *Swift* due to its solar proximity. However, one can clearly see the rise in flux in the *Swift* UVOT bands; likely the onset of a flare the peak of which escaped detection. The radio light curve shows a second flare that accompanies the 2020 outburst detected with *Swift*. A third radio flare of comparable peak flux is also seen in 2021, when the X-rays remained in a rather low state and the optical–UV showed mini-flares superposed on a broader multi-months flare with intermediate peak flux. The two radio flares overlapped to form a broad emission hump. A further, well separated, sharp radio flare is seen in late 2021, reaching the highest flux levels during the whole 2019–2021 time interval of observations. While the optical–UV and X-rays showed a deep low-state throughout 2021 December, the radio flux levels remained high.

While the peak radio flux density of the flares is rather similar (values between 6 and 8 Jy), the peak ratio of the optical over the radio flux varies more strongly among the flares. The second flare has the highest relative optical flux, while the last one has the highest relative radio flux with no particular longer-lasting optical flare event identifiable (Table 4).

Like the radio observations, the *Fermi* gamma-ray light curve is continuous as well, in contrast to ground-based optical and space-based *Swift* data that come with a $\sim$3 month gap due to OJ 287's solar proximity every year. Overall, the *Fermi*-LAT gamma-ray light curve shows a much lower level of activity since 2017 (Fig. A1) than it showed before. The epoch pre-2017 was characterized by several bright and broad gamma-ray flares (e.g. Abdo et al. 2009; Hodgson et al. 2017) with evidence for correlated variability in the radio (millimetre-wave) and gamma-ray band (Agudo et al. 2011). In particular, there is no evidence that the 2020 outburst detected with *Swift* in all wavebands does have a near-simultaneous bright gamma-ray counterpart. Since 2019 (Fig. 6), OJ 287 has been relatively

Table 3. Receivers used in our Effelsberg observations of OJ 287 since 2019 (Effelsberg programme IDs 13-18, 75-19, 65-20, and 70-21). Only the radio frequencies most recently employed since 2019 are listed. (Some receivers have changed in the past, and at selected epochs a larger number of frequencies was observed in the course of the MOMO programme) ν_{centre} is the central frequency, $\Delta\nu$ the band width and HPBW the half power beam width.

Receiver	ν_{centre} (GHz)	$\Delta\nu$ (MHz)	HPBW (arcsec)	Comment
S110 mm	2.595	10	286	
S60 mm	4.85	500	150	
S28 mm	10.45	300	67.5	
S20 mm	14.25	2500	52.9	
	16.75	2500	43.7	
S14 mm	19.25	2500	40.1	S14 included from 2020 April
	21.15	2500	38.0	occasional RFI at 19.25 GHz
	22.85	2500	36.8	
	24.75	2500	33.1	
S7 mm	36.25	2500	23.0	35.75 GHz until MJD 58981 (2020 May 12)
	38.75	2500	21.2	38.25 GHz until MJD 58981 (2020 May 12)
	41.25	2500	20.7	used since 2021 March 24
	43.75	2500	19.7	used since 2021 March 24
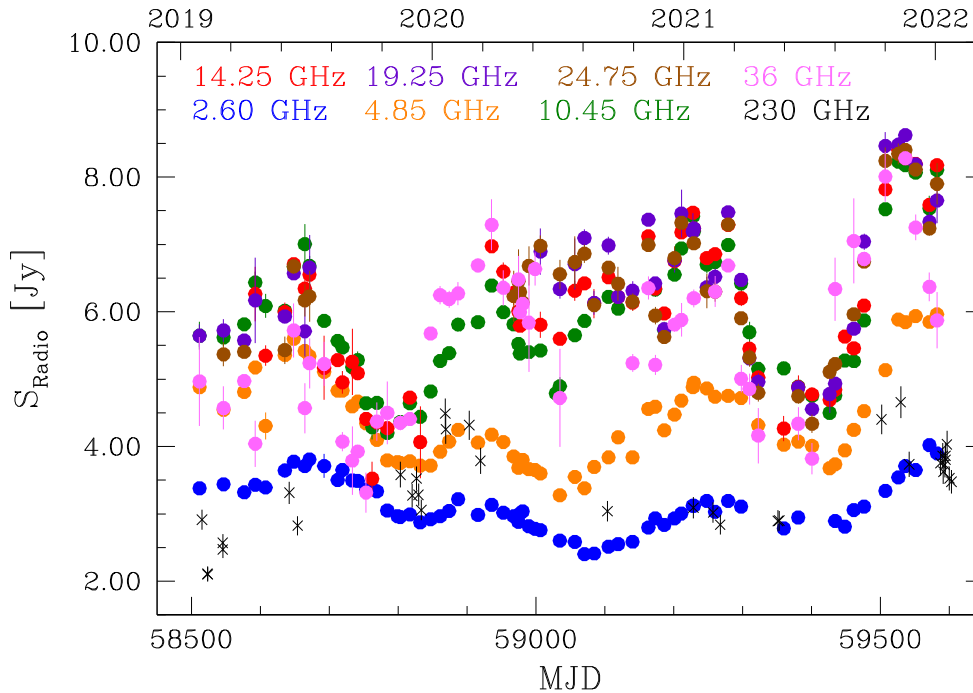
Figure 4. Radio light curves of OJ 287 between 2019 and 2021 measured at the Effelsberg telescope and with the SMA.

inactive at gamma-rays. The highest post-2016 gamma-ray flux was reached around 2021 October 3 at a flux level of 2.11 ($\pm$ 0.26) $^{-4}$ MeV cm^{-2} s^{-1} (3 d average). Given the findings of Agudo et al. (2011), it is possible that the bright gamma-ray flare is associated with the strong radio flare that peaks in mid-November, but ongoing observations of similar events are needed to evaluate their correlation.

5 DISCUSSION

5.1 Activity state of OJ 287 in the radio band

We have caught OJ 287 in a state of high activity in the radio band during the period 2019–2022.04 with several bright flares. The broadband SED from radio to X-rays is shown in Fig. 7.

Radio spectral indices are in the range $\alpha_\nu = -0.38$ to 0.23 at high frequencies (10.45–36 GHz) and higher at low frequencies. Overall, the turnover frequencies of the radio SED have shifted to lower frequencies (10–25 GHz) during the epoch of observations in comparison with Lee et al. (2020) who reported values between 30 and 50 GHz during the earlier epoch 2013–2016, implying that OJ 287 became optically thin at lower frequencies during its recent activity since 2019.

The pronounced radio flare at the end of 2021 is used to estimate the apparent brightness temperature and Doppler factor during that epoch. At 36.25 GHz, and based on a flux doubling time-scale of 135 d, we obtain an apparent brightness temperature of $T_{B,app} = 6.7 \times 10^{12}$ K. Taking the inverse Compton limit of $T = 10^{12}$ K as conservative limit (Kellermann & Pauliny-Toth 1969) and assuming

Table 4. Summary of the properties of the four radio flares at peak. Column entries: (1) Flare designation, (2) peak flux density at 36 GHz, (3) modified Julian date (MJD) of the 36 GHz peak (uncertain by ± 10 d given the observing cadence), (4) calendar date of the 36 GHz peak, (5) MJD of the optical peak, (6) time difference between radio (36 GHz) and optical (*V*) peak in days, (7) ratio of peak fluxes in the optical (*V*) and radio (36 GHz) band, (8) spectral index α_ν at peak (between 10 and 36 GHz), (9) spectral index α_ν between 36 and 225 GHz (observations at these two frequencies are not simultaneous, but agree within 1–7 d except for 16 d at F2).

Flare	$S_{\text{peak, 36GHz}}$ (Jy)	$\text{MJD}_{36\text{GHz}_{\text{peak}}}$	$\text{date}_{36\,\text{GHz}_{\text{peak}}}$	$\text{MJD}_{V_{\text{peak}}}$	$\Delta t_{V-36\,\text{GHz}}$ (d)	$f_V/f_{36\,\text{GHz}}$	$\alpha_{\nu,10-36\,\text{GHz}}$	$\alpha_{\nu,36-225\,\text{GHz}}$
(1)	(2)	(3)	(4)	(5)	(6)	(7)	(8)	(9)
F1	5.72 ± 0.40	58648.557	2019–06–14	58647.964	-0.6	12.2^1	-0.12	-0.30
F2	7.29 ± 0.38	58935.896	2020–03–27	58962.351	$+26.5$	22.5^2	$+0.11$	-0.36
F3	6.20 ± 0.03	59229.138	2021–01–15	59220.480	-8.7	16.3^3	-0.12	-0.38
	6.69 ± 0.05	59278.991	2021–03–05	59284.463	$+5.5$	14.8	-0.03	
F4	8.28 ± 0.11	59536.240	2021–11–18	59530.448^4	-5.8	–	$+0.01$	-0.31

Notes. [1]The last observed *V* flux was used for this ratio, since OJ 287 entered *Swift* Sun constraint afterwards. [2] MJD and flux ratio correspond to the first optical peak of the triple-peaked optical outburst. [3] This broad flare has two optical peaks of similar flux, and both peaks are listed. [4]At this epoch, no clear flare can be defined in the optical–UV. The flux shows some rapid variations by a factor >2. The MJD corresponds to the single highest *V* flux.

a spectral index $\alpha = -1$ of the optically thin part of the radio spectrum then gives a minimum Doppler factor of $\delta = 3.4$ of the emitting component.

We come back to the radio emission in comparison with the other wavebands when discussing epochs of particular interest below.

5.2 Epochs of special interest

During the period 2019–2022.04 that is the focus of this study, several remarkable flux and spectral states of OJ 287 were detected. Some of these coincide in time with predictions from the SMBBH model, while others are likely driven by jet physics independent of any binary's presence. We discuss each of these epochs in turn in the next sections. When we compare with predictions of the binary model of OJ 287, these are based on Lehto & Valtonen (1996) with latest numbers from Dey et al. (2018). In brief, the model predicts impact flares when the secondary SMBH crosses the primary's accretion disc, and after-flares when the impact disturbance reaches the inner disc and triggers changes in jet activity. The flares are not equidistant in time, but their timing changes in a predictable manner, based on the model for the elliptical, precessing orbit of the secondary SMBH. The main flares associated with disc impacts do not become observable immediately but only after a time delay corresponding to the time interval it takes the expanding, impact-driven bubble to become optically thin (Ivanov et al. 1998; Valtonen et al. 2022). Therefore, below, we distinguish between the time of the actual disc impact event, and the later, major 'impact flare'.

Our observations cover two main episodes of predicted SMBBH activity: The epoch of the 2019 impact flare that we cover in the radio band (not with *Swift*, since OJ 287 was in *Swift* Sun constraint), and the epoch of the 2021 December secondary-SMBH disc crossing (the actual predicted impact flare will only be visible later, after the expanding bubble becomes optically thin). We comment on each in turn, in addition to other epochs of interesting flux/spectral states of OJ 287.

5.2.1 Epoch of 2019 July–August and binary impact flare

During mid-2019, the epoch of the latest predicted impact flare, OJ 287 was neither observable from the ground in the NIR-optical regime, nor from space with *Swift*, due to its close proximity to the Sun. The *Spitzer Space Telescope* with its Earth-trailing orbit was used instead and the detection of a (thermal) IR flare at the expected time was reported by Laine et al. (2020).

Our radio monitoring also covered the larger time frame (2019 July–August) and we observed at a higher cadence. During the epoch, a broad radio flare (lasting months) was detected. The flare maximum was reached around 2019 June 14 about 6 weeks before the IR flare detected with *Spitzer* with peak on 2019 July 31 (note, however, that the *Spitzer* flare was interpreted as thermal emission, so the two events are then not directly related). During this epoch there is an interesting inversion of the radio spectrum with flux densities at the higher frequencies as low as at 4.85 GHz and particularly low flux densities at 36 GHz. This is likely at least partly due to opacity-dependent time delays for each frequency band to reach its maximum, with higher frequencies turning down faster than lower frequencies, along with rapid variability at the highest frequency. The spectral inversion persists until October 2019.

During the *Spitzer* IR flare, a short gamma-ray flare was recorded with *Fermi*; the second-brightest *Fermi* flare during 2019 (Fig. 6). The gamma-ray flare peaked quasi-simultaneous with the IR flare on 31 July 2019, suggesting that the two are related.[7]

---

[7]Even though we do not discuss epochs pre-2019 much further here, it is interesting to note that the previous binary impact flare of 2015 December (Valtonen et al. 2016) was accompanied by a gamma-ray flare, too, simultaneous to within a day (Section A, Fig. A1). It was the brightest flare recorded since late 2015. *If* the secondary possessed a jet during its impact (but see Section 5.2.4), then its interaction with the dense accretion disc could be a potential source of gamma-ray emission, in analogy to the gamma-ray production mechanism discussed by Araudo, Bosch-Ramon & Romero (2010), who consider jet interactions with dense broad-line region clouds. Such a scenario could potentially explain the 2019 gamma-ray flare, but not the 2015 gamma-ray flare because 2.39 yr had already passed since the actual disc impact according to the model (Dey et al. 2018; Valtonen et al. 2022), and the secondary SMBH had already crossed the disc when in 2015 the near-side impact-driven bubble became optically thin and the *optical* thermal flare became observable. It is possible, however, that the far-side bubble triggered renewed accretion and jet activity of the secondary's jet with new gamma-ray flaring as a consequence, when interacting with the accretion disc. Mechanisms to produce gamma-ray emission in SMBBH context will be further discussed in future work.
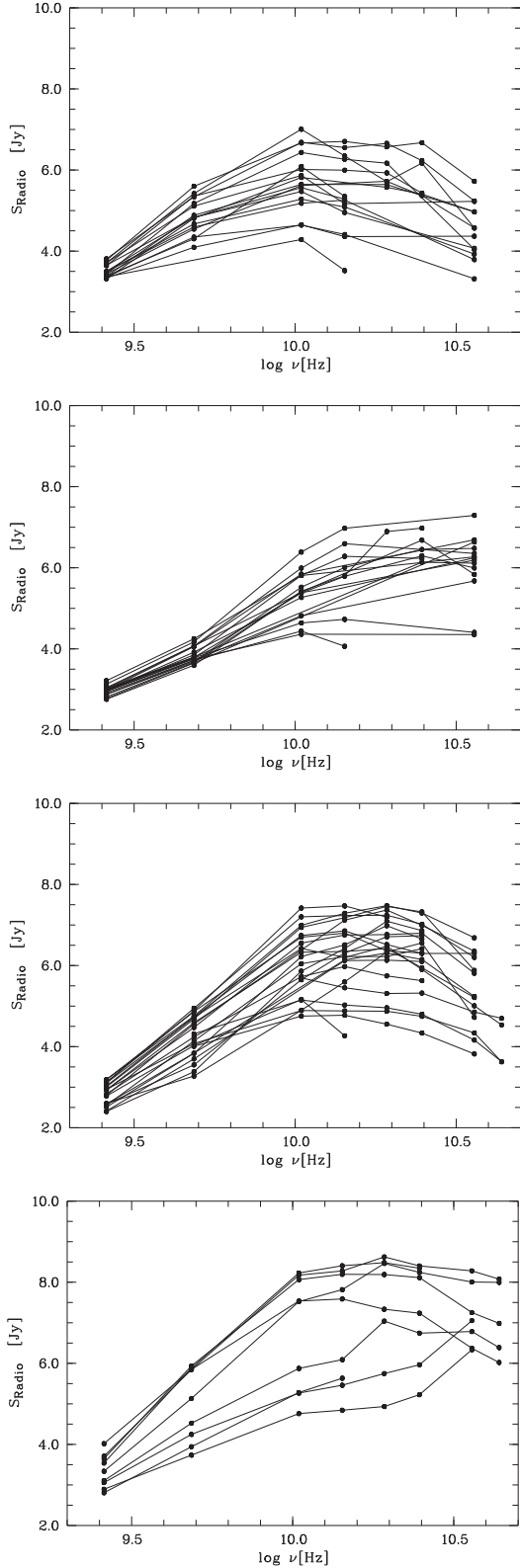
with dedicated deep follow-up observations with XMM-Newton and NuSTAR and their modelling and interpretation, and by Komossa et al. (2021d) in context with the other OJ 287 flux and spectral states of interest since 2005. [Our initial report about the detection of this outburst (ATel #13658) also triggered an additional X-ray observation (Prince et al. 2021; Singh et al. 2021) that still found OJ 287 in the supersoft X-ray state that characterized this outburst.] Here, we only point out that the detection of radio flaring activity independently confirms the previous conclusions about the non-thermal nature of the outburst. In particular, this also supports the previous conclusion that the event is consistent with an after-flare predicted by the binary model (Sundelius et al. 1997), where new jet activity is launched.

5.2.3 The 2020–2021 broad flare

During late 2020 and 2021 a remarkable, long-lasting UV–optical flaring event ('broad flare') is evolving at intermediate emission levels, accompanied by radio flaring. The fractional variability amplitude F_{var} during this epoch (Table 2) is intermediate between previous states of outbursts (2016/2017 and 2020) and states of quiescence of OJ 287 (Siejkowski & Wierzcholska 2017; Komossa et al. 2021d), and significantly higher than the near-zero variability of OJ 287 on sub-day time-scales observed in X-rays with *XMM–Newton* (Gallant, Gallo & Parker 2018; Komossa et al. 2020, 2021d).

During this epoch, the power-law photon index Γ_x is no longer as closely correlated with source count rate, as it was in previous epochs, with an indication of an emerging anti-correlation at the end of 2021, as opposed to the strong correlation so far seen during outburst epochs (e.g. Komossa et al. 2021a) driven by a soft synchrotron component. An anticorrelation can be understood if a hard IC component makes a stronger contribution to the recent X-ray spectra. Future observations are needed to confirm this trend. In previous epochs, the UV and optical emission of OJ 287 has been closely correlated with time lags consistent with $\tau = 0 \pm 1$ d at all activity states of OJ 287. The lag measurements of the epoch 2020 September to 2021 June confirm the near-zero time delay between the optical and UV bands, consistent with the expectations from synchrotron theory (Kirk, Rieger & Mastichiadis 1998).

5.2.4 2021 December optical–UV low-state and secondary SMBH disc crossing

In 2021 December, the UV and optical emission is at a low state. Such long-lasting low-flux states were last reached during the deep fade in 2017 and the 2020 September minimum (Komossa et al. 2020, 2021d). It is interesting to note that this epoch coincides with a secondary SMBH disc impact on 2021 December 3 predicted by the SMBBH model (Valtonen et al. 2022). The related thermal impact *flare* will only become visible in mid-2022 according to the model predictions, once the impact-driven outflow becomes optically thin. However, we may expect enhanced activity due to shocks in the vein of the impact when the secondary encounters high-density material like disc winds or the disc corona prior to the actual disc impact, leading to enhanced emission in the optical to high-energy regime. Whether or not such radiation becomes detectable w.r.t. the bright long-lived non-thermal blazar emission, is another question. Visual inspection of the light curve in 2021 September–December does not reveal any outstanding features. Further, the fractional variability analysis (Table 2) does not find an enhanced variability pattern at that epoch in comparison to the previous epoch.
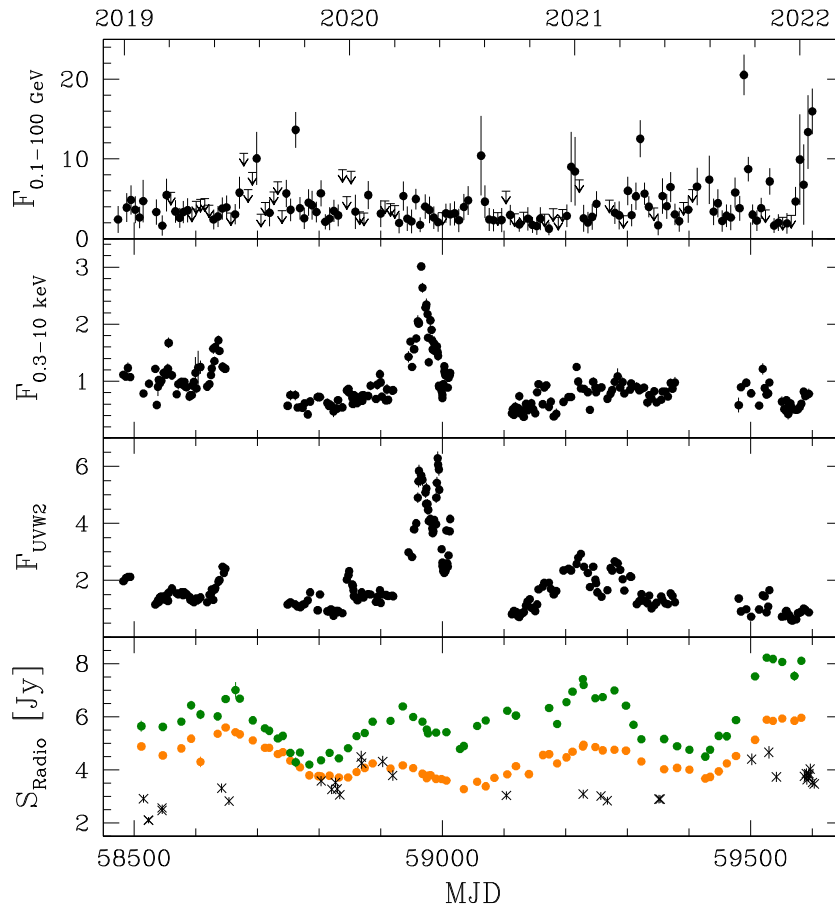

Figure 5. Radio SEDs of OJ 287 between 2019 and 2021 (upper panel 1: MJD 58511–58784, panel 2: MJD 58799–59028, panel 3: MJD 59034–59426, panel 4: MJD 59434–59582). Each panel includes one of the flares.

5.2.2 2020 April–June outburst

This non-thermal outburst was reported and discussed in detail by Komossa et al. (2020) including the initial *Swift* discovery along

Figure 6. OJ 287 light curves from 2019 to 2022.04 in gamma-rays, X-rays, UV–W2, and selected radio frequencies (orange: 4.85 GHz, green: 10.45 GHz, black: 225 GHz). The gamma-ray flux, observed absorption-corrected X-ray flux (0.3–10 keV) and the extinction-corrected optical–UV fluxes are given in units of 10^{-11} erg s^{-1} cm^{-2}. The radio flux density is given in Jy.
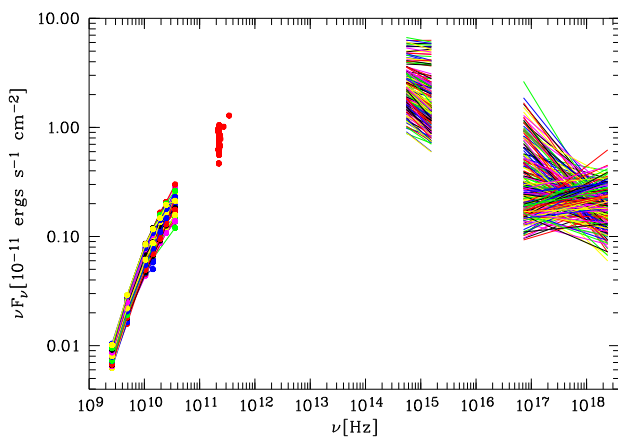

Figure 7. Broadband SEDs of OJ 287 between 2019 and 2021. Simultaneous observations in the UV–optical and in X-rays are presented by the same line colour, even though the colour scheme is meant to merely highlight the range of observed spectra, not any single one in particular. The radio observations are generally not simultaneous with the *Swift* data within hours, and an independent colour scheme is used. Single data points are additionally overplotted in the radio regime, since not all frequencies are covered each time.

Pihajoki et al. (2013b) considered the possibility that the secondary SMBH undergoes accretion, as it approaches the disc surrounding the primary SMBH, including the possibility that the secondary launches a temporary jet. Detailed simulations that address the question whether a classical accretion disc can form (and survive) and whether jet launching is possible under these extreme conditions, while the secondary is moving at relativistic speed through a rapidly changing environment, have not yet been carried out. If a temporary jet does form, then estimates show that it may reach a comparable radio luminosity to the primary jet under favourable conditions (section 8 of Valtonen et al. 2022). Therefore, could the strong radio flare we see rapidly rising in 2021 August be associated with the secondary SMBH? If so, we expect to detect the signature of the temporary accretion disc in the form of a strong X-ray signal. However, X-rays remain at low emission levels since 2021 September (when OJ 287 became observable again with *Swift* after the Sun constraint). Therefore, either there was only a short-lived accretion episode that had already faded in September, while the jet continued to evolve and emit, or, much more likely, the radio emission we detect is from the main jet of OJ 287. One way to test further the secondary jet scenario would be to search the ongoing radio flare for rapid variability/periodicity similar to the period of the last stable orbit (Valtaoja et al. 1985; Pihajoki et al. 2013b).

Back to the UV–optical low state, we may ask if the secondary SMBH's disappearance itself behind the disc could contribute to the observed 2021 UV–optical inactivity directly? This is highly
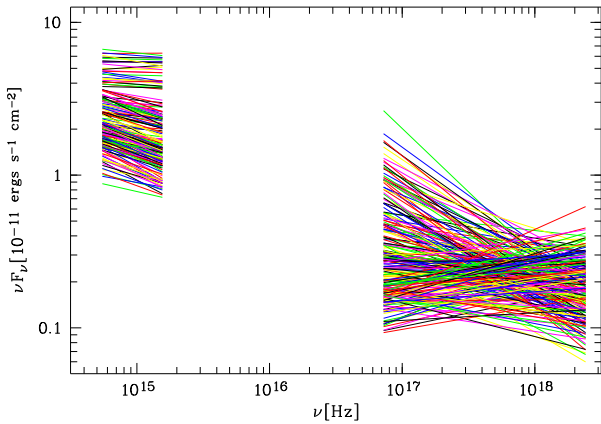
Figure 8. The same SEDs as in Fig. 7, but now a zoom on the UV–X-ray part of the SED. The trend of flatter optical–UV slopes and steeper X-ray slopes as the fluxes increase is evident.
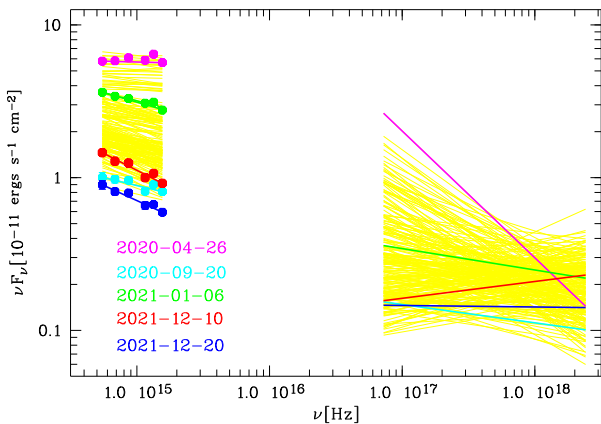

Figure 9. Selected representative broad-band SEDs of OJ 287 from the optical to X-rays, including high-state, low-state, and states close to candidate binary events. The yellow area represents the entirety of SEDs observed since 2019.

unlikely because the broad-band emission of OJ 287 is dominated by the primary SMBH within the context of the binary model, not the secondary, and therefore, its disappearance behind the disc should not dim the observed broad-band emission of OJ 287.

Another way to look at signatures of disc impact is to search for the emergence of a new spectral component during 2021 December.

If a new spectral component and/or a different emission mechanism was prevalent during this epoch, we can expect a change in the UV–optical spectral shape. The optical–UV spectral index $\alpha_{\nu_{V-W2}}$ of OJ 287 is in the range -1.3 to -1.5 during the month of 2021 December. It does not systematically change across the low state (Figs 8 and 9), and it is similar to other epochs at comparable flux low states. We conclude that the low state is driven by jet physics, since there is no evidence that it could have been directly caused by the disc passage of the secondary SMBH in the binary model.

Independent of the mechanism that causes deep minimum states, these states facilitate imaging and photometry of the host galaxy of OJ 287 (Nilsson et al. 2020; Valtonen et al., in preparation) that is otherwise challenging because of the bright emission of the blazar component. In the future, the *James Webb Space Telescope* (Gardner et al. 2006) will be ideally suited to carry out deep host imaging of OJ 287 once a new UV–optical deep fade is detected.

The presence of the deep UV–optical low-state at a time of a high level of activity in the radio band may imply the emergence of a new or additional radio component of different broad-band emission properties. The monitoring of OJ 287 continues to follow the multiband flux evolution.

6 SUMMARY AND CONCLUSIONS

We reported results from our long-term monitoring project of OJ 287, MOMO, based on observations taken at >14 different frequencies from 2.6 GHz to 100 GeV between 2019 and 2022 January, providing exquisite multiwavelength coverage at a cadence as high as one day. MOMO is a long-term project aimed at understanding disc–jet physics as well as testing new predictions of the SMBBH model of this nearby bright blazar, with the long-term goal of covering densely at least one binary orbital period of 12 yr.

The main results of this latest publication in a sequence can be summarized as follows:

(i) OJ 287 is found in a high activity phase in the radio regime with four major flare events. Turnover frequencies are low and in the range of 10–25 GHz. Using the sharpest, brightest flare in late 2021, an apparent brightness temperature $T_{B, app} = 6.7 \times 10^{12}$ K and a minimum Doppler factor $\delta_{min} = 3.4$ are estimated.

(ii) The radio–optical SED is highly variable, with strong changes in the optical/radio flux ratio of individual flare events. The well-observed non-thermal 2020 outburst (Komossa et al. 2020) stands out as the one with the highest optical/radio peak flux ratio, while the major radio flare peaking in November 2021 only has a faint optical counterpart, if any.

(iii) Unlike the pre-2017 observations that were characterized by several bright, multiweek gamma-ray flares, the activity in the gamma-ray band has been relatively low post-2017. The two noteworthy events are (1) a gamma-ray flare that is simultaneous within a day with the *Spitzer* IR flare (Laine et al. 2020) of 2019 July 31 and (2) the brightest gamma-ray flare since 2015 that was recorded in early 2021 October.

(iv) Two structures of special interest have been identified in the 2020–2021 light curves. First, a remarkable, long-lasting 'broad flare' in the UV–optical and radio bands with indications of an emerging reversal of the previous Γ_x–CR correlation. The reversal can be understood if IC emission makes an increased contribution to X-rays. The second epoch of interest is a deep optical–X-ray low state in 2021 December at the time of a disc crossing event predicted by the SMBBH model.

The project MOMO continues to follow the flux and spectral evolution of OJ 287 in coming years.

and reverence that the summit of Maunakea has always had within the indigenous Hawaiian community. We are most fortunate to have the opportunity to conduct observations from this mountain. This work made use of data supplied by the UK Swift Science Data Centre at the University of Leicester. This work has made use of *Fermi*-LAT data supplied by Kocevski et al. 2021, https://fermi.gsfc.nasa.gov/ssc/data/access/lat/LightCurveRepository/. This research has made use of the NASA/IPAC Extragalactic Database (NED) which is operated by the Jet Propulsion Laboratory, California Institute of Technology, under contract with the National Aeronautics and Space Administration.

DATA AVAILABILITY STATEMENT

Reduced data are available on reasonable request. The raw data of our project are available in the *Swift* data archive at https://swift.gsfc.nasa.gov/archive/.

REFERENCES

Abdo A. A. et al., 2009, ApJ, 700, 597
Agudo I. et al., 2011, ApJ, 726, L13
Araudo A. T., Bosch-Ramon V., Romero G. E., 2010, A&A, 522, 97
Arnaud K. A., 1996, ASPC, 101, 17
Atwood W. B. et al., 2009, ApJ, 697, 1071
Ballet J. et al., 2020, preprint (arXiv:2005.11208)
Begelman M. C., Blandford R. D., Rees M. J., 1980, Nature, 287, 307
Blandford R. D., Meier D., Readhead A., 2019, ARA&A, 57, 467
Breeveld A. A. et al., 2010, MNRAS, 406, 1687
Britzen S. et al., 2018, MNRAS, 478, 3199
Burrows D. N. et al., 2005, SSRv, 120, 165
Cardelli J. A., Clayton G. C., Mathis J. S., 1989, ApJ, 345, 245
Ciprini S. et al., 2007, MmSAI, 78, 741
Colpi M., 2014, SSRv, 183, 189
Comastri A., Molendi S., Ghisellini G., 1995, MNRAS, 277, 297
de Rosa A. et al., 2019, New Astron. Rev., 86, 101525
Dey L. et al., 2018, ApJ, 866, 11
Dey L. et al., 2021, MNRAS, 503, 4400
Edelson R. A., Krolik J. H., 1988, ApJ, 333, 646
Edelson R. et al., 2017, ApJ, 840, 41
Evans P. et al., 2007, A&A, 469, 379
Event Horizon Telescope Collaboration, 2019, ApJ, 875, L1
Fuhrmann L. et al., 2016, A&A, 596A, 45
Gallant D., Gallo L. C., Parker M. L., 2018, MNRAS, 480, 1999
Gardner J. P. et al., 2006, SSRv, 123, 485
Gehrels N. et al., 2004, ApJ, 611, 1005
Graham M. J. et al., 2015, Nature, 518, 74
Grupe D. et al., 2010, ApJS, 187, 64
Gurwell M. A., Peck A. B., Hostler S. R., Darrah M. R., Katz C. A., 2007, in ASP Conf. Ser. Vol. 375, From Z-Machines to ALMA: (Sub)Millimeter Spectroscopy of Galaxies. Astron. Soc. Pac., San Francisco, p. 234
Heeschen D. S. et al., 1987, AJ, 94, 1493
Hill J. E. et al., 2004, Proc. SPIE, 5165, 217
Hodgson J. A. et al., 2017, A&A, 597, A80
Idesawa E. et al., 1997, PASJ, 49, 631
Ivanov P. B., Igumenshchev I. V., Novikov I. D., 1998, ApJ, 507, 131
Kalberla P. M. W. et al., 2005, A&A, 440, 775
Kapanadze B. et al., 2018, MNRAS, 480, 407
Katz J. I., 1997, ApJ, 478, 527
Kellermann K. I., Pauliny-Toth I. I. K., 1969, ApJ, 155, L71
Kirk J. G., Rieger F. M., Mastichiadis A., 1998, A&A, 333, 452
Kocevski D., Valverde J., Garrappa S., Negro M., Brill A., Ballet J., Lott B., 2021, Astron. Telegram, 15110, 1
Komossa S. et al., 2015, Astron. Telegram, 8411, 1
Komossa S., Baker J. G., Liu F. K., 2016, IAU Focus Meeting, 29B, 292
Komossa S. et al., 2017, IAUS, 324, 168 (paper I)

Komossa S. et al., 2020, MNRAS, 498, L35 (paper II)
Komossa S. et al., 2021a, MNRAS, 504, 5575 (paper III)
Komossa S. et al., 2021b, Publ. Astron. Obs. Belgrade, 100, 29
Komossa S. et al., 2021c, Universe, 7, 261 (paper IVa)
Komossa S. et al., 2021d, ApJ, 923, 51 (paper IVb)
Kraus A. et al., 2003, A&A, 401, 161
Laine S. et al., 2020, ApJ, 894, L1
Lee J. W. et al., 2020, ApJ, 902, 104
Lehto H. J., Valtonen M. J., 1996, ApJ, 460, 207
Liska M., Hesp C., Tchekhovskoy A., Ingram A., van der Klis M., Markoff S., 2018, MNRAS, 474, L81
Lister M. L. et al., 2013, AJ, 146, 120
Liu F. K., Wu X. B., 2002, A&A, 388, L48
Madejski G. M., Schwartz D. A., 1988, ApJ, 330, 776
Marscher A. P., Jorstad S. G., 2011, ApJ, 729, 26
Massaro E. et al., 2003, A&A, 399, 33
Massaro E. et al., 2008, A&A, 489, 1047
Moretti A. et al., 2005, Proc. SPIE, 5898, 360
Myserlis I. et al., 2018, A&A, 619, A88 (paper Ib)
Nilsson K. et al., 2020, ApJ, 904, 102
O'Brien S., 2017, Proc. 35th International Cosmic Ray Conference (ICRC 2017). preprint (arXiv:1708.02160)
Pihajoki P., Valtonen M., Ciprini S., 2013a, MNRAS, 434, 3122
Pihajoki P. et al., 2013b, ApJ, 764, 5
Poole T. S. et al., 2008, MNRAS, 383, 627
Prince R. et al., 2021, MNRAS, 508, 315
Pursimo T. et al., 2000, A&AS, 146, 141
Qian S. J., 2015, RAA, 15, 687
Rieger F. M., 2004, ApJ, 615, L5
Roming P. W. A. et al., 2005, SSRv, 120, 95
Roming P. W. A. et al., 2009, ApJ, 690, 163
Sambruna R. M. et al., 1994, ApJ, 434, 468
Schlegel D. J., Finkbeiner D. P., Davis M., 1998, ApJ, 500, 525
Sesana A., 2021, FrASS, 8, 7
Seta H. et al., 2009, PASJ, 61, 1011
Siejkowski H., Wierzcholska A., 2017, MNRAS, 468, 426
Sillanpää A. et al., 1988, ApJ, 325, 628
Sillanpää A. et al., 1996, A&A, 315, L13
Singh K. P. et al., 2021, preprint (arXiv:2110.14978)
Smith P. S. et al., 1987, ApJS, 64, 459
Stroh M. C., Falcone A. D., 2013, ApJS, 20, 28
Sundelius B. et al., 1997, ApJ, 484, 180
Timmer J., König M., 1995, A&A, 300, 707
Valtaoja E. et al., 1985, Nature, 314, 148
Valtaoja E. et al., 2000, ApJ, 531, 744
Valtonen M. J., Sillanpää A., 2011, AcPol, 51, 76
Valtonen M. J. et al., 2016, ApJ, 819, L37
Valtonen M. J. et al., 2019, ApJ, 882, 88
Valtonen M. J. et al., 2022, Galaxies, 10, 1
Vaughan S., Edelson R., Warwick R. S., Uttley P., 2003, MNRAS, 345, 1271
Villata M. et al., 1998, MNRAS, 293, L13
Villforth C. et al., 2010, MNRAS, 402, 2087
Volonteri M., Haardt F., Madau P., 2003, ApJ, 582, 559
Wehrle A. E., Carini M., Wiita P. J., 2019, ApJ, 877, 151
Williamson K. E. et al., 2014, ApJ, 789, 135
Wilms J., Allen A., McCray R., 2000, ApJ, 542, 914
Wright E. L., 2006, PASP, 118, 1711
Yao S., Komossa S., 2021, MNRAS, 501, 1384
Yardley D. R. B. et al., 2010, MNRAS, 407, 669
Zola S. et al., 2016, Galaxies, 4, 41

APPENDIX: ADDITIONAL LIGHT CURVES

Fig. A1 displays the 2015 December to 2021 December light curve of OJ 287 from the MOMO project, showing the most recent measurements in the long-term context, and including the *Fermi*
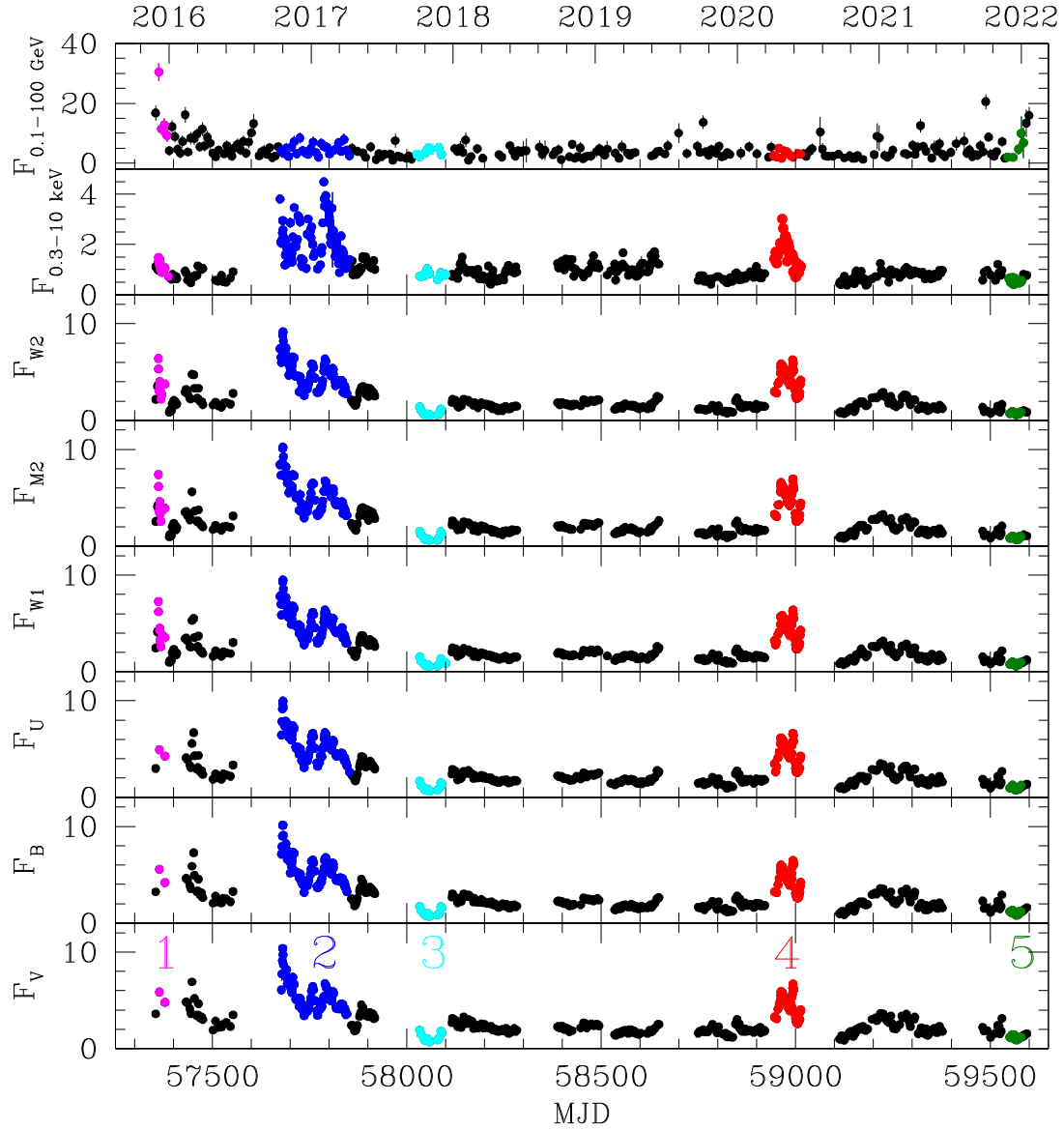
Figure A1. *Fermi* gamma-ray and *Swift* X-ray to optical light curve of OJ 287 from 2015 December 1 to 2022 January 15. For previous versions of this light curve, see Komossa et al. (2017, 2020). Panels, from top to bottom: (1) gamma-ray flux between 0.1–100 GeV in units of 10^{-11} erg s^{-1} cm^{-2}; (2) absorption-corrected 0.3–10 keV X-ray flux in units of 10^{-11} erg s^{-1} cm^{-2}; (3–8) extinction-corrected UVOT UV and optical fluxes at each filter's central wavelength in units of 10^{-11} erg s^{-1} cm^{-2}. Error bars are always plotted but are often smaller than the symbol size. Selected epochs are marked in colour: (1) The epoch of the optical high-state in December 2015 interpreted as an impact flare in the binary model (Valtonen et al. 2016, pink). Note that it is associated with a gamma-ray flare. (2) The epoch of the bright 2016–2017 synchrotron outburst (Komossa et al. 2020, dark blue). (3) The epoch of the remarkable, symmetric UV–optical deep fade (Komossa et al. 2021d, light blue). (4) The epoch of the 2020 synchrotron outburst (Komossa et al. 2020, 2021a, red) consistent with an after-flare predicted by the binary model. (5) The epoch of the UV–optical low-state in 2021 December (section 6.3.4; green) that coincides in time with the binary model prediction of a disc-crossing of the secondary SMBH (Valtonen et al. 2022).

data for the whole epoch. Particular events are marked in colour including the two major outbursts in 2016/2017 and 2020, the deep low-states in 2017 and 2021, and the episode of enhanced optical–UV activity in 2015 December. The latter is associated with a *Fermi* flare that coincides in time (within 1 d) with the sharp, bright optical flare reported by Valtonen et al. (2016) [note that the

optical peak was highest in a ground-based observation (Valtonen et al. 2016) and was not caught exactly at that maximum with *Swift*; Fig. A1].

In Fig. A2, the *Swift* and *Fermi* observations of OJ 287 during the year 2021 are highlighted, resolving the flux evolution during this epoch in better detail than the long-term light curves.
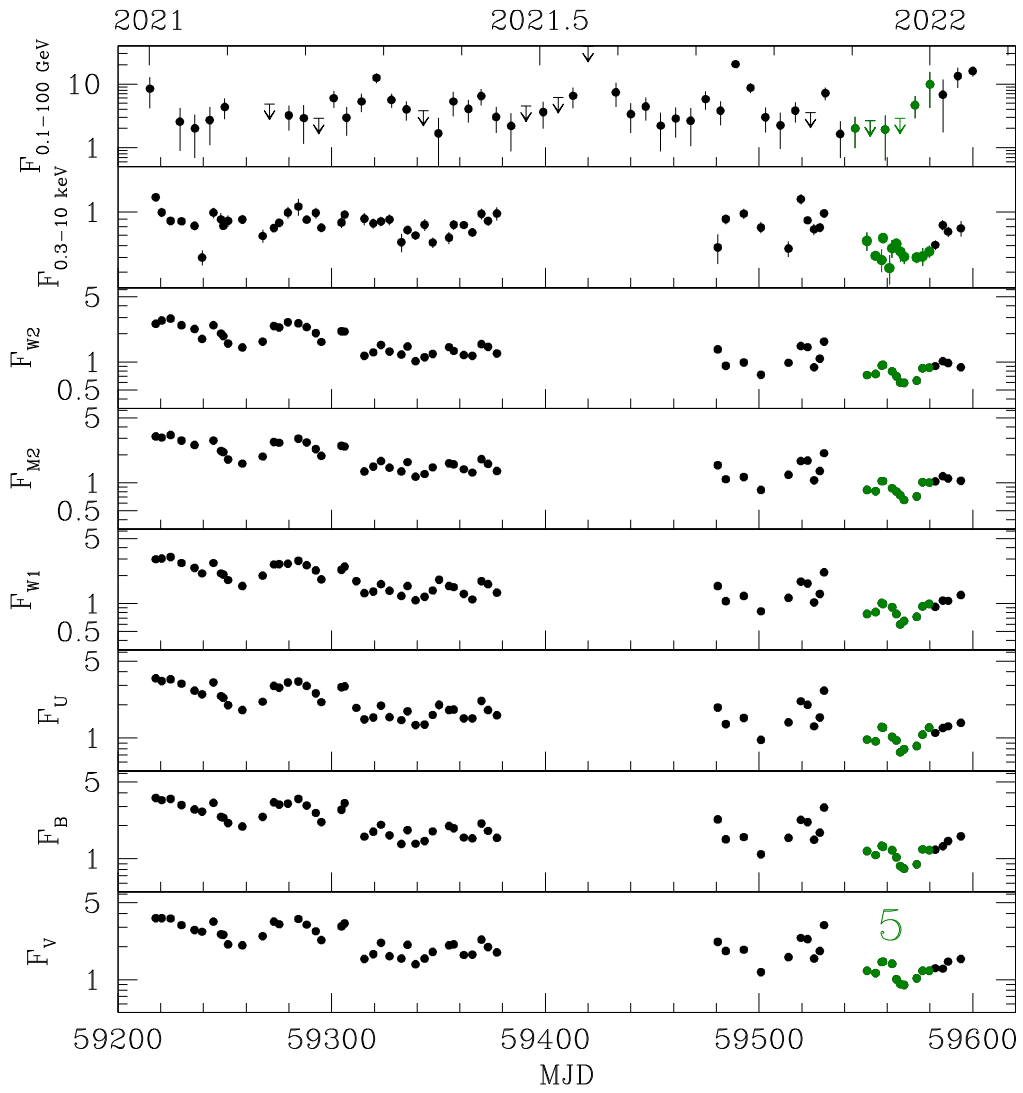
Figure A2. 2021–2022.04 *Swift* and *Fermi* light curve of OJ 287. Units as in Fig. A1.

This paper has been typeset from a TₑX/LAᵀₑX file prepared by the author.